Published in final edited form as:

Phys Med Biol. 2009 May 7; 54(9): 2885–2899. doi:10.1088/0031-9155/54/9/020.

Performance evaluation of an Inveon PET preclinical scanner

Cristian C Constantinescu and **Jogeshwar Mukherjee**

Department of Psychiatry and Human Behavior, University of California Irvine, Irvine, CA, USA

Cristian C Constantinescu: constant@uci.edu

Abstract

We evaluated the performance of an Inveon preclinical PET scanner (Siemens Medical Solutions), the latest MicroPET system. Spatial resolution was measured with a glass capillary tube (0.26 mm inside diameter, 0.29 mm wall thickness) filled with ^{18}F solution. Transaxial and axial resolutions were measured with the source placed parallel and perpendicular to the axis of the scanner. The sensitivity of the scanner was measured with a ^{22}Na point source, placed on the animal bed and positioned at different offsets from the center of the field of view (FOV), as well as at different energy and coincidence windows. The noise equivalent count rates (NECR) and the system scatter fraction were measured using rat-like (Φ = 60, L = 150 mm) and mouse-like (Φ = 25 mm, L = 70 mm) cylindrical phantoms. Line sources filled with high activity ^{18}F (>250 MBq) were inserted parallel to the axes of the phantoms (13.5 and 10 mm offset). For each phantom, list-mode data were collected over 24 h at 350–650 keV and 250–750 keV energy windows and 3.4 ns coincidence window. System scatter fraction was measured when the random event rates were below 1%. Performance phantoms consisting of cylinders with hot rod inserts filled with ^{18}F were imaged. In addition, we performed imaging studies that show the suitability of the Inveon scanner for imaging small structures such as those in mice with a variety of tracers. The radial, tangential and axial resolutions at the center of FOV were 1.46 mm, 1.49 and 1.15 mm, respectively. At a radial offset of 2 cm, the FWHM values were 1.73, 2.20 and 1.47 mm, respectively. At a coincidence window of 3.4 ns, the sensitivity was 5.75% for EW = 350–650 keV and 7.4% for EW = 250–750 keV. For an energy window of 350–650 keV, the peak NECR was 538 kcps at 131.4 MBq for the rat-like phantom, and 1734 kcps at 147.4 MBq for the mouse-like phantom. The system scatter fraction values were 0.22 for the rat phantom and 0.06 for the mouse phantom. The Inveon system presents high image resolution, low scatter fraction values and improved sensitivity and count rate performance.

1. Introduction

Interest in applying positron emission tomography (PET) to animal models of normal and disease states has grown rapidly. The field, with initial emphasis on general markers of metabolic activity and blood flow, has progressed with the introduction of methodologies for imaging neurotransmitter systems and gene expression, and for aiding the drug development (Gambhir *et al* 2000, Wang and Maurer 2005). PET is minimally invasive and facilitates serial and longitudinal studies to be performed in the same animal, thus reducing the number of animals required for each study. One of the major impediments for the use of PET with small animals is the small physical dimensions of the subjects, especially the brain. While chemical selectivity of PET tracers is well established, and the mass sensitivity to extremely low, trace concentrations of radiopharmaceuticals is unsurpassed, the spatial resolution of clinical human PET scanners are poorly suited to animal imaging (Vaquero and Desco 2005). The best human system is the high-resolution research tomograph (HRRT), which has a resolution of

Correspondence to: Cristian C Constantinescu, constant@uci.edu.

approximately 2.5 mm (Boellaard *et al* 2003). Many dedicated small animal PET cameras have been developed and their physical characteristics and performance have been previously discussed (Schafers 2003, Weber and Bauer 2004). Among them, the systems in the MicroPET series offer excellent sensitivity and good resolution at the same time. Previous MicroPET systems include P4 and Focus 220 for imaging primates and R4 and Focus 120 for imaging rodents (Tai *et al* 2001, Knoess *et al* 2003, Tai *et al* 2005, Kim *et al* 2007, Laforest *et al* 2007).

An Inveon dedicated PET scanner is the latest commercially available small animal PET system developed by Siemens Medical Solutions, Inc. Compared to previous MicroPET systems, it presents an increased axial field of view (FOV) and features better light guide design and improved signal processing electronics which are aimed toward increasing sensitivity, improving the data transmission and shortening the dead time. The system allows docking to SPECT and CT modules to create a multimodality system with components operating independently under the control of the same data acquisition computer.

In this work, we have performed an independent evaluation of the performance of the Inveon system that was installed at University of California Irvine in the fall of 2007. Parameters defining the image resolution, sensitivity, scatter fraction and counting loss performance have been measured.

2. Materials and methods

2.1. System description

Inveon is a ring-type, high-sensitivity PET scanner intended for imaging small animals, such as mice and rats. Its detector array consists of 64 detector blocks (16 transaxial and 4 axial) arranged circularly. Each detector module is placed in time coincidence with opposite modules to give an effective transaxial FOV of approximately 10 cm and an axial FOV of 12.7 cm. Each detector module consists of a 20 × 20 array of LSO crystals of size 1.5 × 1.5 × 10 mm on a 1.59 mm crystal pitch and with an average depth of interaction of 4.58 mm. The LSO block is optically coupled to a position-sensitive photomultiplier tube (Hamamatsu R8900 C12 PSPMT) via a tapered multiple-element light guide (Mintzer and Siegel 2007). The system is equipped with a new high-speed event processing and routing architecture called Quicksilver™. It consists of ring-based event processing modules (EPMs) with digital communication transmitting event packets that use a ‘store and forward’ concept. Each EPM performs coincidence determination around the ring, thus eliminating the need for separate coincidence processing electronics. The event routing subsystem (ERS) for acquisition and processing has two transport interfaces for acquiring events: an IEEE 1394 A interface and a PCI interface (Newport *et al* 2006).

A Co-57 retractable point source is used to acquire transmission data which serve for attenuation correction. PET data are acquired in list mode, and list-mode data can be sorted into three-dimensional (3D) sinograms using different span numbers and ring differences or directly into two-dimensional (2D) sinograms by single-slice rebinning (SSRB) (Daube-Witherspoon and Muehllehner 1987). The images can be reconstructed in 2D by applying the filtered backprojection (FBP) or 2D ordered-subset expectation maximization (OSEM 2D) to the 2D sinograms resorted by either the Fourier rebinning algorithm (FORE) (Defrise *et al* 1997) or SSRB. Reconstruction can also be done directly from the 3D sinograms using a 3D reprojection (3DRP) algorithm (Kinahan and Rogers 1989), 3D ordered subset expectation maximization (OSEM 3D) (Yao *et al* 2000) or a maximum *a posteriori* (MAP) algorithm in conjunction with OSEM 3D (Nuyts *et al* 1999). A comparison of Inveon specifications with those of two other previous MicroPET systems, R4 and Focus 120 is provided in table 1.

2.2. Spatial resolution

The spatial resolution of the system was measured with a glass capillary tube (ID = 0.26 mm, 0.29 mm wall thickness) filled with 14.8 MBq of ^{18}F according to NEMA recommendations (National Electrical Manufacturers Association 2007). The source was attached to an optical filter holder placed on the animal bed. Transaxial resolution was measured with the source placed parallel to the axis of the scanner. The data were collected as a function of the position of the source as it was moved radially toward the edge of the transaxial FOV in 1 mm steps covering a distance between 0 and 45 cm from the center of FOV. The acquisition time at each source position was 60 s. The number of random coincidences in every acquisition was less than 5% of the number of prompt coincidences. The number of true coincidences was between 15 million and 63 million. A 350–650 keV energy window and 3.43 ns timing window were used for data acquisition. The data were sorted into sinograms of span 3 and ring difference 79. Random events were subtracted prior to rebinning. The images were reconstructed using FORE and 2D FBP with a ramp filter with a frequency cutoff at Nyquist frequency. The size of the image matrix was 1024 × 1024 × 159 resulting in a pixel size of 0.097 mm and a slice thickness of 0.796 mm. No attenuation correction was applied. Both FWHM and FWTM of the count profiles were computed by linear interpolation between adjacent pixels at half and one-tenth of the maximum value, respectively. The maximum value for each profile was calculated using parabolic interpolation of the highest three values. The width of each profile in the direction perpendicular to that of measurement was equal to at least two times the FWHM of the orthogonal direction. For measurement of axial resolution, the capillary tube, filled with 7.4 MBq of ^{18}F, was placed perpendicular to the axis of the scanner. For each radial position, three different axial measurements were performed by moving the source along the axis of the scanner in steps equal to one-third of the slice thickness (0.265 mm) (Tai *et al* 2003). The axial profiles at the three source positions were interleaved in order to obtain oversampled axial profiles that were used to calculate the axial FWHM and FWTM. The radial offsets for the axial resolution measurements covered only a range between 0 and 40 cm from the center because of physical limitations imposed by the geometry of the source holder combined with the vertical bed motion.

2.3. Sensitivity

The sensitivity was measured using a 603.1 kBq ^{22}Na point source (Eckert & Ziegler Isotope Products) with a nominal size of 0.3 mm encapsulated in a plastic cube with a side of 10 mm. The source was placed on the scanner bed, centered in the transaxial FOV and stepped toward the end of the axial FOV starting at the center. Once the source reached the end of the axial FOV, it was returned to the center and stepped in the opposite direction. The step size was equal to 0.097 mm, representing the slice thickness. The acquisition time was set to 2 s for each measurement to ensure the collection of at least 100 000 true events with a random to true event rate ratio of less than 1%. The average acquisition time recorded in each sinogram header was 2.6 ± 0.2. The background rate was measured by acquiring an image in the absence of the source for an acquisition time equal to that used to acquire the source data in the center of the FOV. The data were sorted in sinograms using SSRB. For each angle of the sinogram, the highest value was identified and all pixels located 1 cm away from the peak value were set to 0. No corrections for scatter or subtraction of random events were applied. The count rate for each slice was measured by dividing the total number of counts in the masked sinogram by the acquisition time. The background count rate was calculated using the same procedure. The sensitivity was calculated as $S=\frac{R-R_B}{A_{\mathrm{cal}}}$ (in cps kBq^{-1}), where R is the source count rate, R_B is the background rate and A_{cal} is the source activity. The absolute sensitivity, S_A, was calculated as $S_A=\frac{S}{0.906}\times 100$, where 0.906 is the branching ratio for positron emission of ^{22}Na. Measurements were performed for two different energy windows (350–650 keV and 250–750 keV) and four different coincidence windows (2.8, 3.4, 4 and 4.7 ns).

In order to map the sensitivity throughout the entire FOV of the scanner, the axial measurements were repeated at four more transaxial positions, with the source positioned at 1, 2, 3 and 4 cm away from the center axis of the scanner. Because of the geometrical restrictions imposed by the curved scanner bed, only half of the transaxial FOV was covered.

In addition, system sensitivity was measured using a line source (length 13 cm; inside diameter, 0.8 mm; outside diameter, 1.6 mm) filled with 26.7 MBq of ^{18}F. We employed a method that was first introduced in Bailey *et al* (1991) and is similar to the one described in detail in NEMA NU-2 2007 (National Electrical Manufacturers Association 2007). In brief, the line source was placed in the center of the transaxial FOV, parallel to the center axis of the scanner and scanned for 120 s each time after being surrounded successively by aluminum sleeves (15 cm long, 1 mm thick) of different diameters. The sleeves created an added shielding thickness of 1, 2, 3, 4 and 5 mm, respectively. The procedure was performed at two energy windows (350–650 keV and 250–750 keV) and 3.4 ns coincidence window. The coincidence events were sorted in sinograms using SSRB. Background and random coincidences were subtracted. The true coincidence count rate in the absence of any attenuation was calculated from the semi-logarithmic plot of the true coincidence count rates versus different shield thicknesses. The system sensitivity was computed from dividing the count rate by the activity in the line source at the time of measurement. For computation of the absolute system sensitivity, the ^{18}F branching factor (0.967) was considered. The slice sensitivities were also computed as recommended in National Electrical Manufacturers Association (2007) using the count rates from the smallest Al tube.

2.4. Scatter fraction and count loss measurements

The noise equivalent count rates (NECR) and the system scatter fraction (SF) were estimated using rat-like (diameter, 60 mm; length, 150 mm) and mouse-like (diameter, 25 mm; length, 70 mm) cylindrical phantoms made of high-density polyethylene (HDPE). Lines sources (inside diameter, 1.0 mm, outside diameter, 1.6 mm) filled with high activity ^{18}F (>250 MBq) were inserted parallel to the axes of the phantoms (13.5 and 10.0 mm offset, respectively) through a 2 mm channel.

List-mode data were collected over 24 h at two energy windows (350–650 keV and 250–750 keV) and 3.4 ns coincidence window for each phantom. Recommendations from NEMA standard NU-4 2008 were followed for measurements of both NECR and scatter fraction (National Electrical Manufacturers Association 2008). The list-mode data were sorted in dynamic sinograms (72 × 5 min, 108 × 10 min) using SSRB. The prompts and the random events were recorded in separate sinograms. The random coincidences were measured using a delayed window method. Each prompt sinogram held at least 500 000 prompt counts. No normalization and corrections for dead time, scatter or attenuation were applied. For both prompt and random sinograms, the pixels located further than 8 mm from the edges of the phantom were set to 0. Further, for each projection angle in the prompt sinograms, the projections were shifted so that the pixel containing the maximum value was aligned with the center of the sinogram. After alignment, a sum projection was computed resulting in a projection with a defined peak corresponding to the line source. The pixel values outside a 14 mm wide strip at the center of the sinogram were considered as entirely due to scatter and random events. The average of the pixel values at +7 mm from the center of the sinogram were multiplied by the number of pixels between the edges of the 14 mm wide strip. The result was added to the counts outside the strip to provide the total number of scatter and random events. The remaining counts in the sum projection were considered true events and used in calculation of the true event count rate. The total number of prompt events in the sinogram, which includes the true, the scattered and the random events, was calculated by summing up all the pixel values in the sum projection. The random coincidence rates were calculated directly from the random events sinograms. NECR values were computed for each acquisition, *i*, using the following equation:

$$\mathrm{NECR}(i)=\frac{R_{\mathrm{true}}^{2}(i)}{R_{\mathrm{total}}(i)},$$

where $R_{\mathrm{true}}(i)$ and $R_{\mathrm{total}}(i)$ are the true and the prompt coincidence count rates for the *i*th acquisition. The counting loss due to dead time was also evaluated from the rat phantom data acquired at 350–650 keV energy window and 3.4 ns coincidence window. This count-loss percentage was defined as $\left(R_{\mathrm{true}}^{\mathrm{extrap}}-R_{\mathrm{true}}\right)/R_{\mathrm{true}}^{\mathrm{extrap}}\times 100$, where $R_{\mathrm{true}}^{\mathrm{extrap}}$ is the expected true coincidence rate that was calculated from fitting a line to the first five data points of lowest activity (Laforest *et al* 2007).

Two different methods were used for calculation of SF. First, system SF was computed from the late acquisitions for which the random event rate was below 1% of the true event rate and it was assumed that the prompt events consisted only of true and scattered events. The SF for each slice was calculated by summing the ratios between the scatter and total number of counts over the low activity acquisitions. The system scatter fraction was computed as a weighted average of slice SF values. Alternatively, for a more accurate measurement of the scatter fraction count rates, the intrinsic radioactivity due to the presence of ^{176}Lu in the scintillation material of the detectors was taken into account (Watson *et al* 2004). The intrinsic counting rate, R_{int}, was measured using the same phantoms and the same scanner settings in the absence of radioactivity in the line sources. Data were acquired for 14 h such that each slice contained at least 50 000 intrinsic counts. The scatter event rate for a frame *i* and slice *j* was calculated as $R_{\mathrm{scatter}}(i,j)=R_{\mathrm{total}}(i,j)-R_{\mathrm{true}}(i,j)-R_{\mathrm{random}}(i,j)-R_{\mathrm{int}}(j)$. The system scatter fraction for each acquisition, *i*, is calculated as $SF(i)=\frac{R_{\mathrm{scatter}}(i)}{R_{\mathrm{true}}(i)+R_{\mathrm{scatter}}(i)}$, where $R_{\mathrm{scatter}}(i)$ is the scattered event rate for the *i*th acquisition, resulted from summing $R_{\mathrm{scatter}}(i,j)$ over all slices. The system scatter fraction with intrinsic radiation correction was reported as the value of SF at five times the amount of total activity that generated a singles count rate equal to that of the intrinsic singles rate.

2.5. Imaging studies

2.5.1. Phantom studies—Two cylindrical phantoms (Data Spectrum Corp.) with hot spot inserts arranged in six segments were scanned with an energy window of 350–650 keV and a coincidence window of 3.42 ns. The first phantom was a Micro Deluxe (inside diameter 4.5 cm, channel length 6.3 cm) with hollow channel diameters of 1.2, 1.6, 2.4, 3.2, 4.0 and 4.8 mm. The second phantom was an Ultra Micro Hot Spot phantom (inside diameter 2.8 cm, channel length 0.99 cm) with hollow channels diameters of 0.75, 1.0, 1.35, 1.7, 2.0, and 2.4 mm. Both phantoms were filled with ^{18}F (25.1 MBq and 55.8 MBq) and scanned for 1 h. The PET images were reconstructed using the 3DRP algorithm (Kinahan and Rogers 1989) with a pixel size of 0.388 × 0.388 mm in a 256 × 256 matrix.

2.5.2. Animal studies—In order to investigate the scanner's capability to image small animals, we imaged three C57 BL/6 J mice with three different radiotracers. One mouse was administered 18.5 kBq of ^{18}F-sodium fluoride via IV tail injection, anesthetized with 1.5% isoflurane following 1 h of awake uptake and then scanned for 30 min. Images were reconstructed using four different algorithms: 2D FBP (ramp filter, cutoff at Nyquist frequency) preceded by Fourier rebinning of the 3D sinograms, 3DRP (no filter), OSEM 2D (16 subsets, 4 iterations) and fast OSEM3D/MAP (2 OSEM3D iterations, 18 MAP iterations). All images were 128 × 128 pixels with a 0.77 mm pixel size. The second mouse was injected with 32.2 MBq of ^{18}F-FDG and scanned for 60 min, starting at 70 min post-injection. The animal was fasted for 24 h before ^{18}F-FDG administration. A third mouse was injected IV with 32.7 MBq of ^{18}F-fallypride (dopamine D2/D3 radioligand) and was imaged for 150 min. In addition to the emission scans, transmission images were acquired for each animal using the Co-57 source and attenuation maps were constructed after sorting in sinograms using SSRB. All animal images were reconstructed using FBP with a ramp filter and cutoff at Nyquist frequency.

3. Results

3.1. Spatial resolution

The radial, tangential and axial resolution (FWHM) at the center of FOV were 1.46 mm, 1.49 and 1.15 mm, respectively. At a radial offset of 2 cm, the FWHM values were 1.73, 2.20 and 1.47 mm, respectively. A plot of radial, tangential and axial resolution as a function of radial offset is presented in figure 1(A). Volumetric resolution versus radial offset is shown in figure 1(B).

3.2. Sensitivity

The sensitivity (absolute sensitivity) measured with the ^{22}Na point source in the center of the FOV was 52.14 cps kBq^{-1} (5.75%) for an energy window of 350–650 keV and coincidence window 3.4 ns and 67.08 cps kBq^{-1} (7.40%) for an energy window of 250–750 keV and coincidence window 3.4 ns. Absolute sensitivity values for the ^{22}Na source placed at four different positions in the FOV and for all combinations of energy windows (350–650 keV, 250–750 keV) and coincidence windows (2.8, 3.4, 4, 4.7 ns) are presented in detail in table 2. A mesh plot of the absolute sensitivity profile throughout the FOV is shown in figure 2 for an energy window of 350–650 keV and 3.4 ns. Using the ^{18}F line source, the system sensitivity values were 29.35 cps kBq^{-1} (3.04%) for an energy window of 350–650 keV and coincidence window of 3.4 ns and 39.31 cps kBq^{-1} (4.07%) for an energy window of 250–750 keV and coincidence window of 3.4 ns. The axial sensitivity profile in cps kBq^{-1} for both energy windows are presented in figure 3.

3.3. Scatter fraction and count loss measurements

The peak true and NECR and the scatter fraction values for both phantoms (rat, mouse) and energy windows (250–750 keV, 350–650 keV) are presented in table 3. For an energy window of 350–650 keV, the peak NECR for the mouse-like and rat-like phantoms were 1734 kcps at 147.4 MBq and 538 kcps at 131.4 MBq, respectively. The peak true count rates were 2056 kcps at 166.2 MBq (mouse phantom) and 910 kcps at 174.7 MBq (rat phantom), respectively. The NECR curves as a function of total activity for both mouse-like and rat-like phantoms are shown in figure 4. From the rat phantom data, the activity that generated 50% count-loss percentage due to dead time was found to be 113.9 MBq (3.1 mCi). The system scatter fraction values at an energy window of 350–650 keV were 0.07 (7%) for the mouse phantom and 0.23 (23%) for the rat phantom. When intrinsic radioactivity was taken into consideration, the scatter fractions were 0.22 (22%) and 0.64 (6.4%), respectively.

3.4. Imaging studies

Phantom images are presented in figure 5. The 1.6 mm hot spots in Micro Deluxe phantom (panel A) were all separated as illustrated by the profile shown in panel B. The 1.2 channels can also be distinguished visually. The 1.35 mm hot spots in the Ultra Micro phantom (panel C) can also be distinguished while the 1.0 mm and 0.75 mm spots could not be discriminated.

The bone images acquired with ^{18}F and presented in figure 6 show a comparable resolution when FBP, 3DRP and OSEM are used and a marked improvement with OSEM3D/fast MAP.

In the ^{18}F-FDG images shown in figure 7(A) of the mouse, the heart can be clearly distinguished and the ventricular walls could be resolved. The ^{18}F-fallypride images (figure 7(B)) clearly show the striata, indicating that Inveon can be used for imaging the small structures in neuroreceptor studies in very small animals such as mice.

4. Discussion

A direct comparison between the performance parameters that we measured for Inveon with those of other small animal systems is not exact because of differences in the source geometries and materials used as well as slight differences in the methods. Table 4 provides a basis for comparison between the parameters we measured for Inveon and those for Focus 120 as reported independently by two different groups (Kim *et al* 2007,Laforest *et al* 2007).

The radial and tangential resolution of Inveon (1.46 mm and 1.49 mm, respectively) were lower than those reported for Focus 120 (1.18 mm and 1.13 mm in Kim *et al* (2007) or 1.36 mm and 1.32 mm in Laforest *et al* (2007)) but the axial resolution was better (1.15 mm for Inveon versus 1.45 mm for Focus 120 from Kim *et al* (2007) or 1.32 mm from Laforest *et al* (2007)). It is important to note that we used a ^{18}F capillary source for these measurements as recommended in National Electrical Manufacturers Association (2007), while the other studies used ^{22}Na point sources of various diameters (0.25 mm in Kim *et al* (2007) and 0.5 mm in Laforest *et al* (2007)). We did not perform any corrections for the size and shape of the source, or for non-collinearity of positron emission. The axial resolution and tangential resolution vary slowly with the radial offset. This explains why the volumetric resolution of Inveon, while lower in the center of the FOV than that of Focus 120, is actually higher at 2 cm radial offset. The high value in the axial resolutions we measured could be in part attributed to the adaptive FORE algorithm included in the Inveon Acquisition Workplace (IAW 1.0.4) software. The algorithm weighs the lines of response (LOR) corresponding to large ring differences less than the lines of response from small ring differences, thus reducing the effect of axial parallax and improving the axial resolution. The transaxial resolution, and especially the radial resolution, degrades as the radial offset increases mainly because of larger differential in the depth of interaction which leads to larger transaxial parallax errors.

The sensitivity values for a central point source can be estimated as two times the system sensitivity computed with the ^{18}F line source (Seidel *et al* 2000, Knoess *et al* 2003). Based on this approximation, the calculated sensitivity values for a centered point source were 6.07% for an energy window of 350–650 keV and coincidence window of 3.4 ns and 8.13% for an energy window of 250–750 keV and coincidence window of 3.4 ns. These values are higher than those reported for Focus 120, based on the measurements with ^{18}F line source and using the same approximation. However, these values appear to slightly overestimate those measured directly with a ^{22}Na point source placed in the center of the FOV (5.75% and 7.40%, respectively). It is important to note that we were not able to measure the sensitivity at a coincidence window larger than 4.7 ns as the coincidence windows for the Inveon are restricted by the manufacturer within the [2.8 4.7] ns interval. As can be noted from examining data in table 2, the sensitivity values did not appreciably vary with the change in the coincidence window. The markedly increased sensitivity of Inveon compared to the previous MicroPET scanner is partially due to improved light collection efficiency provided by the shorter light guides that features multiplexed coupling to the scintillator array elements and by the PSPMT which is a better version than that used in Focus 120 detectors (Mintzer and Siegel 2007).

Our peak sensitivity value for an energy window of 250–750 keV is lower than the value advertised by the manufacturer (10%). The exact method and materials that the manufacturer used for measuring sensitivity has not been published. It could be speculated that the difference may arise from the histogramming of the data and the use of different number of LORs. We histogrammed the list data for sensitivity measurements using SSRB as recommended in the NEMA 2008 document but we used the IAW 1.0.4 default values of 3 for the span (one direct and 2 oblique planes) and 79 for the maximum ring difference. It is expected that the utilizations of complete set of line of responses (maximum span and maximum ring difference) will increase the measured higher sensitivity.

The scatter fraction and peak NECR were measured using HDPE cylindrical phantoms with the same size as those described in Laforest *et al* (2007). Based on direct comparison with the values reported in that study, the scatter fraction of Inveon for the mouse-like phantom was lower than that of Focus 120, while that for the rat-like phantom was slightly higher. The peak NECR for both phantom types was much higher than that of Focus 120 and it was reached earlier because of the increased sensitivity of Inveon. The improved counting rate capability could be attributed to the use of novel Quicksilver architecture with coincidence events that are transmitted between EPM and ERS for acquisition and processing at rates of up to 1.9 million coincidence events per second. In addition, the PCI interface of the ERS can support up to 16.7 million events per second (Newport *et al* 2006). The energy resolution, an important performance parameter, has not been measured in this work. The manufacturer has reported an average energy resolution of 18%.

5. Conclusions

We have evaluated the performance of an Inveon dedicated PET scanner by measuring the spatial resolution, sensitivity, scatter fraction and count rate performance. Inveon presents higher sensitivity and improved count rate performance over all previous MicroPET systems. These improvements are beneficial to imaging small animals such as mice and rodents using low doses of radiotracers.

Acknowledgments

This work was supported by NIH through grant S10RR019269-01A2 from the National Center for Research Resources (NCRR) and grant R01 EB006110-01A2 from the National Institute of Biomedical Imaging and Bioengineering (NIBIB). The authors would like to thank Robert Coleman for valuable help with preparing and handling the animals for imaging.

References

Bailey DL, Jones T, Spinks TJ. A method for measuring the absolute sensitivity of positron emission tomographic scanners. Eur J Nucl Med 1991;18:374–9. [PubMed: 1879443]

Boellaard R, Buijs F, de Jong HW, Lenox M, Gremillion T, Lammertsma AA. Characterization of a single LSO crystal layer high resolution research tomograph. Phys Med Biol 2003;48:429–48. [PubMed: 12630740]

Daube-Witherspoon ME, Muehllehner G. Treatment of axial data in three-dimensional PET. J Nucl Med 1987;28:1717–24. [PubMed: 3499493]

Defrise M, Kinahan PE, Townsend DW, Michel C, Sibomana M, Newport DF. Exact and approximate rebinning algorithms for 3-D PET data. IEEE Trans Med Imaging 1997;16:145–58. [PubMed: 9101324]

Gambhir SS, et al. Imaging transgene expression with radionuclide imaging technologies. Neoplasia 2000;2:118–38. [PubMed: 10933072]

Kim JS, Lee JS, Im KC, Kim SJ, Kim SY, Lee DS, Moon DH. Performance measurement of the microPET focus 120 scanner. J Nucl Med 2007;48:1527–35. [PubMed: 17704248]

Kinahan PE, Rogers JG. Analytic 3D image-reconstruction using all detected events. IEEE Trans Nucl Sci 1989;36:964–8.

Knoess C, et al. Performance evaluation of the microPET R4 PET scanner for rodents. Eur J Nucl Med Mol Imaging 2003;30:737–47. [PubMed: 12536244]

Laforest R, Longford D, Siegel S, Newport DF, Yap J. Performance evaluation of the microPET (R)—FOCUS-F120. IEEE Trans Nucl Sci 2007;54:42–9.

Mintzer, RA.; Siegel, SB. Design and performance of a new pixelated-LSO/PSPMT gamma-ray detector for high resolution PET imaging. IEEE Nuclear Science Symp. Conf. Record IEEE; 2007. p. 3418-22.

National Electrical Manufacturers Association. NEMA Standards Publication NU 2-2007: Performance Measurements of Positron Emission Tomographs. 2007.

National Electrical Manufacturers Association. NEMA Standards Publication NU 4-2008: Performance Measurements of Small Animal Positron Emission Tomographs. 2008.

Newport, DF.; Siegel, SB.; Swann, BK.; Atkins, BE.; McFarland, AR.; Pressley, DR.; Lenox, MW.; Nutt, RE. QuickSilver: a flexible, extensible, and high-speed architecture for multi-modality imaging. IEEE Nuclear Science Symp. Conf. Record; 2006. p. 2333-4.

Nuyts J, Dupont P, Stroobants S, Benninck R, Mortelmans L, Suetens P. Simultaneous maximum a posteriori reconstruction of attenuation and activity distributions from emission sinograms. IEEE Trans Med Imaging 1999;18:393–403. [PubMed: 10416801]

Schafers KP. Imaging small animals with positron emission tomography. Nuklearmedizin 2003;42:86–9. [PubMed: 12802469]

Seidel, J.; Vaquero, JJ.; Lee, IJ.; Green, MV. Experimental estimates of the absolute sensitivity of a small animal PET scanner with depth-of-interaction capability. IEEE Nuclear Science Symp. and Medical Imaging; Piscataway, NJ. 2000.

Tai YC, Chatziioannou A, Siegel S, Young J, Newport D, Goble RN, Nutt RE, Cherry SR. Performance evaluation of the microPET P4: a PET system dedicated to animal imaging. Phys Med Biol 2001;46:1845–62. [PubMed: 11474929]

Tai YC, Chatziioannou AF, Yang Y, Silverman RW, Meadors K, Siegel S, Newport DF, Stickel JR, Cherry SR. MicroPET II: design, development and initial performance of an improved microPET scanner for small-animal imaging. Phys Med Biol 2003;48:1519–37. [PubMed: 12817935]

Tai YC, Ruangma A, Rowland D, Siegel S, Newport DF, Chow PL, Laforest R. Performance evaluation of the microPET focus: a third-generation microPET scanner dedicated to animal imaging. J Nucl Med 2005;46:455–63. [PubMed: 15750159]

Vaquero JJ, Desco M. Technical limitations of the positron emission tomography (PET) for small laboratory animals. Rev Esp Med Nucl 2005;24:334–47. [PubMed: 16194469]

Wang J, Maurer L. Positron emission tomography: applications in drug discovery and drug development. Curr Top Med Chem 2005;5:1053–75. [PubMed: 16181131]

Watson CC, Casey ME, Eriksson L, Mulnix T, Adams D, Bendriem B. NEMA NU 2 performance tests for scanners with intrinsic radioactivity. J Nucl Med 2004;45:822–6. [PubMed: 15136632]

Weber S, Bauer A. Small animal PET: aspects of performance assessment. Eur J Nucl Med Mol Imaging 2004;31:1545–55. [PubMed: 15517252]

Yao R, Seidel J, Johnson CA, Dube-Witherspoon ME, Green MV, Carson RE. Performance characteristics of the 3-D OSEM algorithm in the reconstruction of small animal PET images. Ordered-subsets expectation-maximixation. IEEE Trans Med Imaging 2000;19:798–804. [PubMed: 11055803]

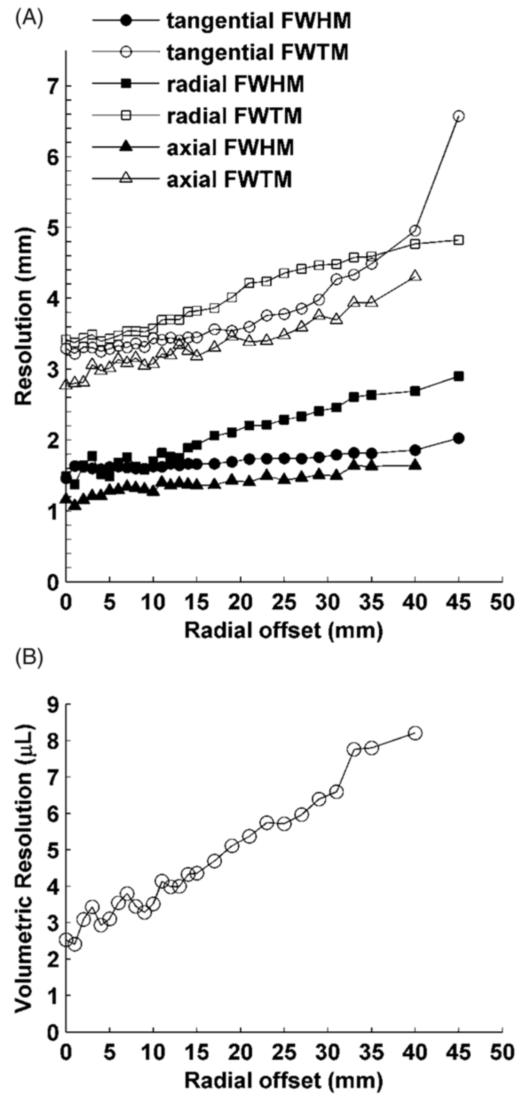

Figure 1.
Image resolution of the Inveon scanner versus radial offset from the center of FOV. (A) FWHM (open markers) and FWTM (filled markers) of the radial, tangential and axial profiles of the ^{18}F source were calculated. (B) Volumetric resolution (product of radial, tangential and axial FWHM) versus radial offset from the center of FOV.

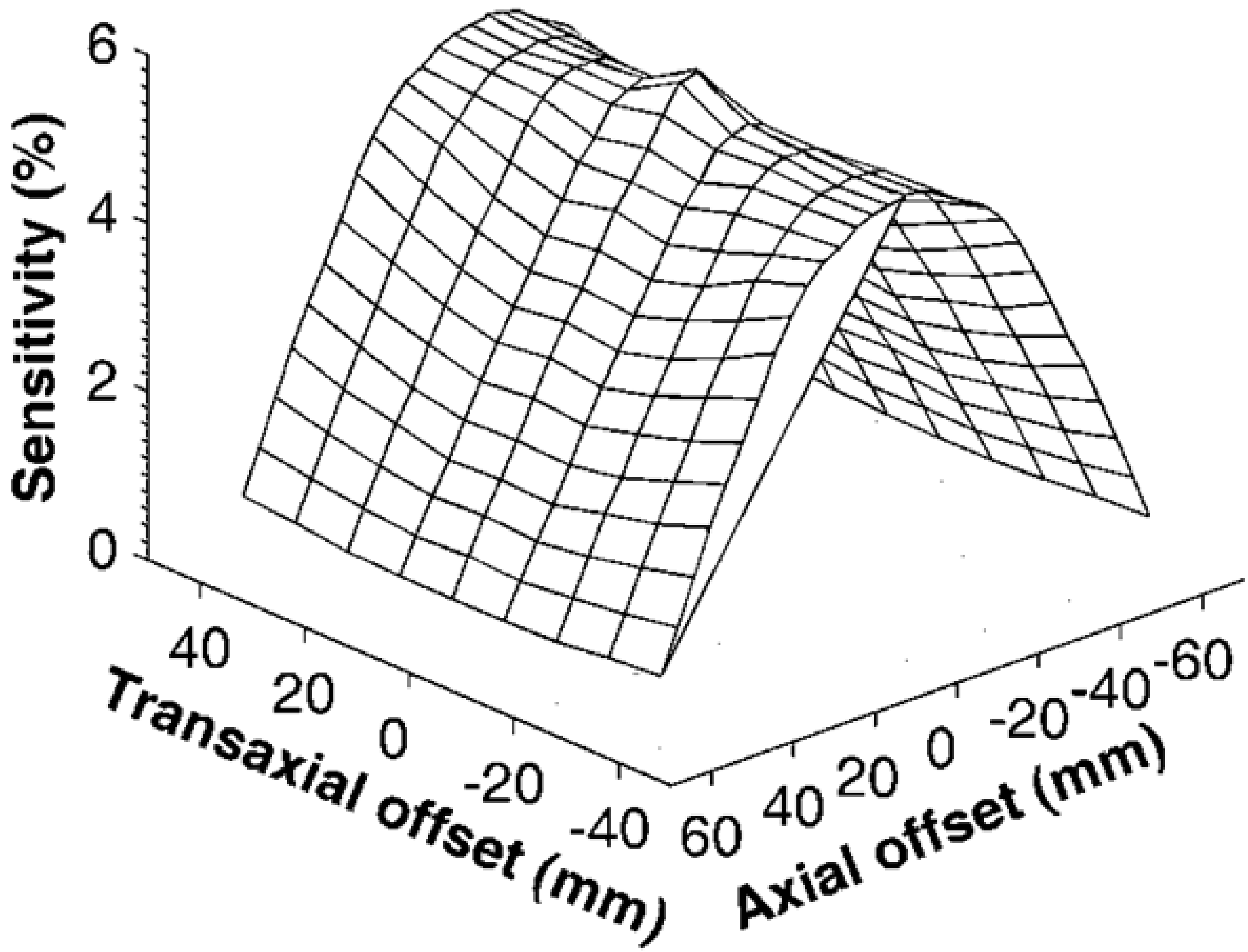

Figure 2.
3D sensitivity profile throughout Inveon FOV as a function of transaxial and axial offset from the center of FOV for a 350–650 keV energy window and 3.4 ns coincidence window.

NIH-PA Author Manuscript
NIH-PA Author Manuscript

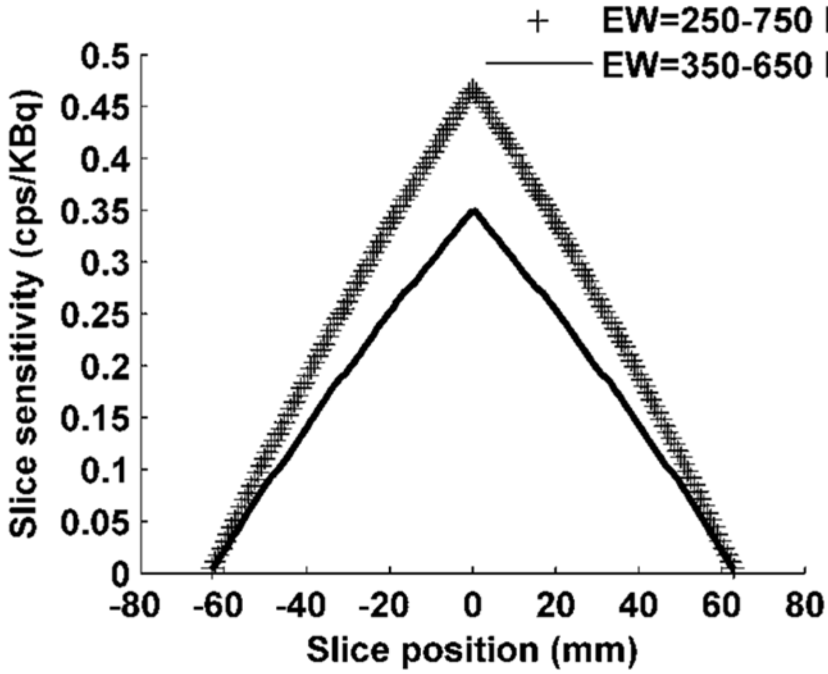

Figure 3.

Axial sensitivity profile measured at two energy windows (250–750 keV, 350–650 keV) and 3.43 ns coincidence window.

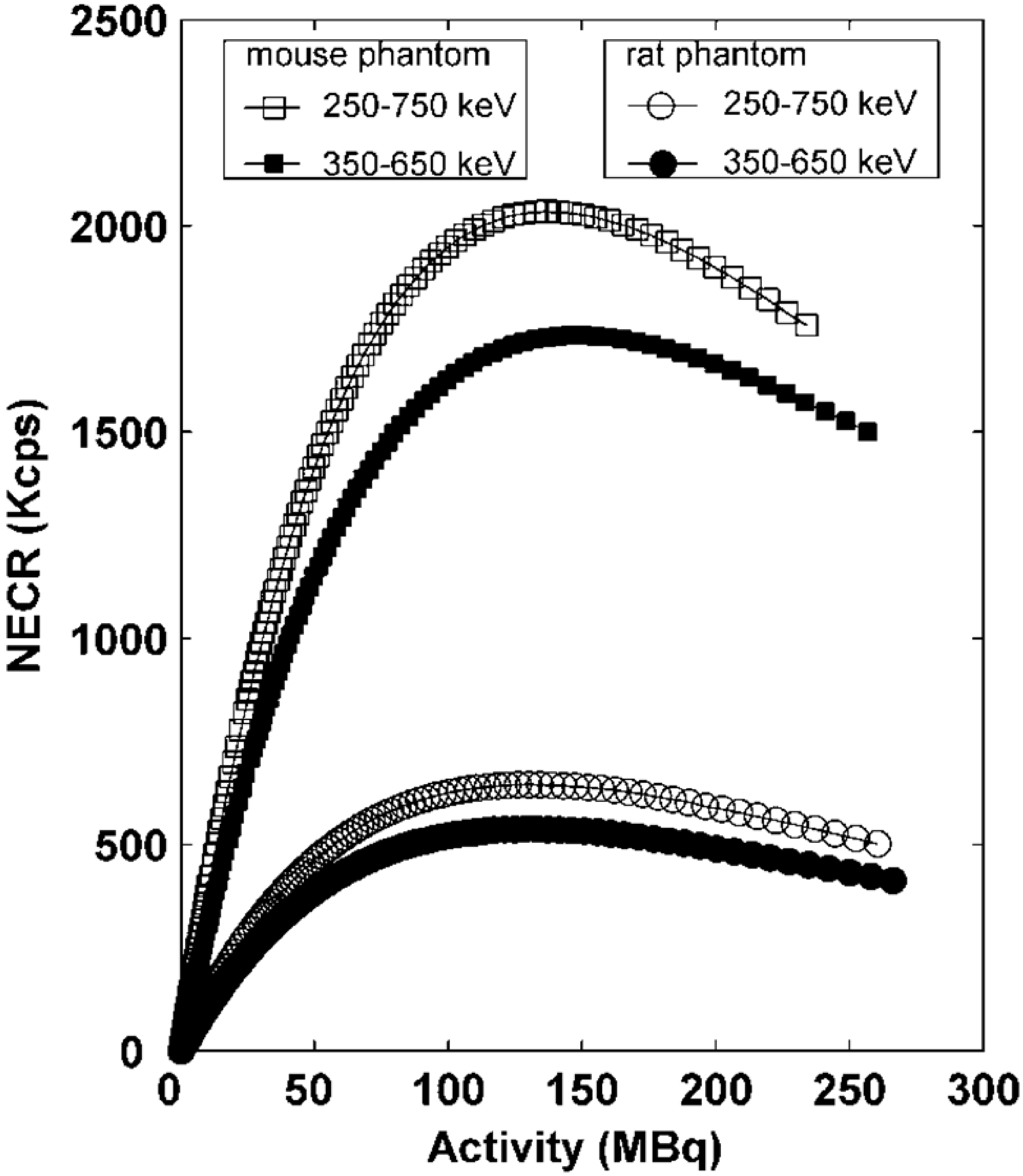

Figure 4.

Noise-equivalent count rate as a function of activity. Data for both rat-like (open and filled circles) and mouse-like (open and filled squares) phantoms are shown. Data were acquired at two different energy windows for each phantom (350–650 keV, 250–750 keV) and 3.4 ns coincidence window.

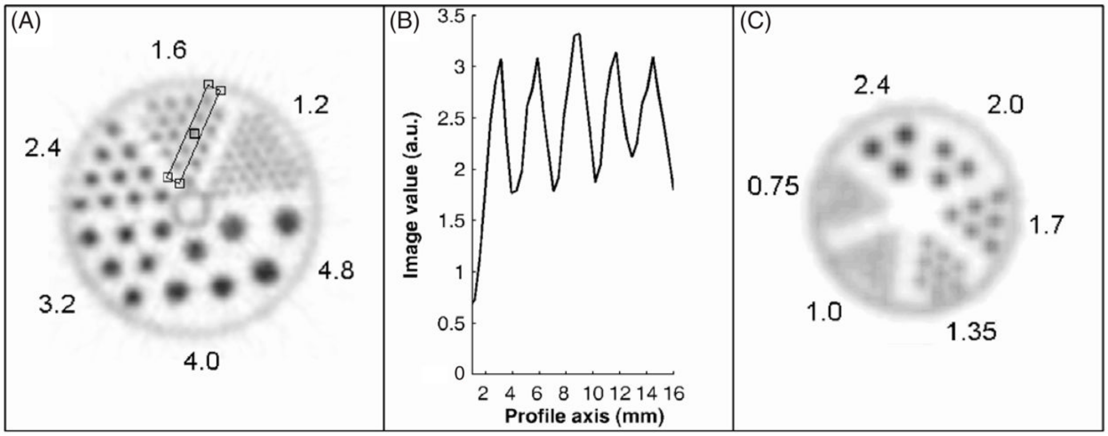

Figure 5.

Transversal (axial) images of (A) Micro Deluxe and (C) Ultra Micro Deluxe hot spot phantoms filled with ^{18}F. The diameter (in mm) of each hollow channel is indicated in the figure. Images were reconstructed using 3DRP algorithm. (B) Profile through a row of 1.6 mm hot spots in the Micro Deluxe phantom. The profile is shown in image (A).

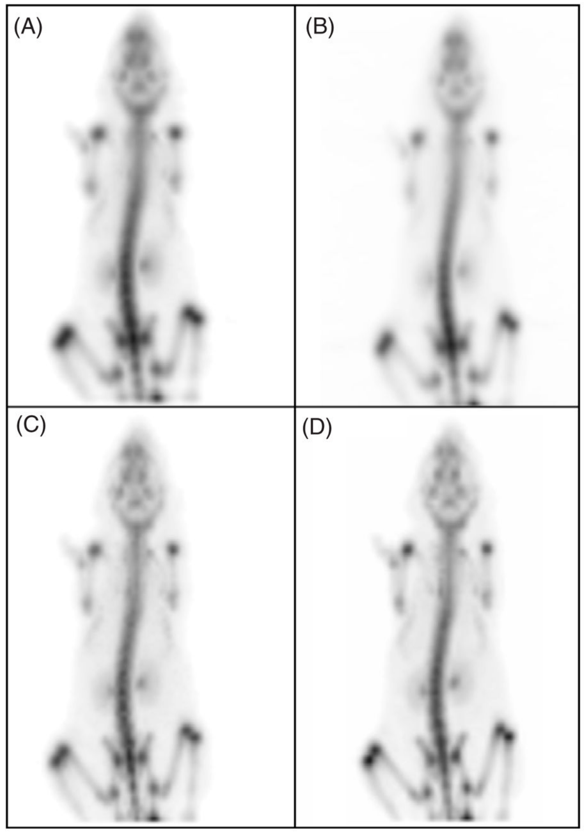

Figure 6.
Maximum intensity projection (MIP) ^{18}F images of a mouse. The images were reconstructed using (A) 2D filtered backprojection (FBP), (B) 3D ordered-subsets expectation maximization (OSEM), (C) 3D-reprojection (3DRP) and (D) maximum *a posteriori* (MAP) algorithms.

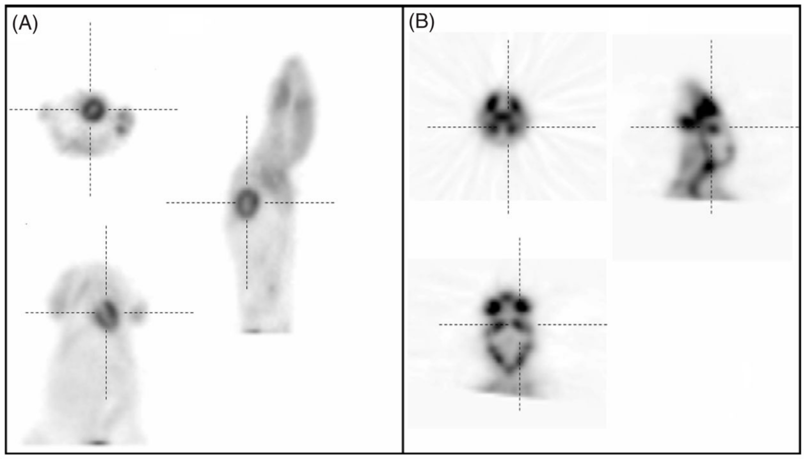

Figure 7.

Mouse images acquired with Inveon scanner. (A) Heart images of a mouse injected with ^{18}F-FDG and scanned for 60 min, starting at 40 min post-injection. Crosshair is positioned on the heart. (B) ^{18}F-fallypride images of a mouse brain scanned for 150 min. Crosshair is positioned on the right striatum. Axial, sagital and coronal views are shown clockwise. Crosshair lines indicate the position of each orthogonal slice. All images were reconstructed with a 2D filtered backprojection algorithm (FBP) following Fourier rebinning.

Table 1

Inveon specifications and comparison with previous MicroPET systems.

Category	Specification	Inveon[a]	Focus 120[b]	R4[c]
Detector	Crystal material	LSO	LSO	LSO
	Crystal element size (mm^3)	1.5 × 1.5 × 10	1.5 × 1.5 × 10	2.1 × 2.1 × 10
	Crystal pitch (mm)	1.59	1.59	2.45
	Crystal array	20 × 20	12 × 12	8 × 8
Scanner	Number of detector blocks	64	96	96
	Number of crystal elements	25 600	13 824	6144
	Bore diameter (cm)	12	12	12
	Transaxial FOV (cm)	10	10	10
	Axial FOV (cm)	12.7	7.6	7.6

[a] Siemens Medical Solutions.

[b] Kim *et al* (2007).

[c] Knoess *et al* (2003).

Table 2

Absolute sensitivity values for a ^{22}Na point source placed at four different positions in the FOV. For each source position, sensitivity values are reported for two different energy windows (350–650 keV, 250–750 keV) and four different coincidence windows, (2.8, 3.4, 4, 4.7 ns). System sensitivity calculated from the measurements with an ^{18}F line source is listed in the far right column.

Axial distance (mm)	Radial distance (mm)	Energy window (keV)	Coincidence window (ns)	Absolute sensitivity (^{22}Na source) (%)	System sensitivity (^{18}F source) (%)
0	0	350–650	2.8	5.72	–
			3.4	5.75	3.04
			4	5.75	–
			4.7	5.75	3.04
		250–750	2.8	7.40	–
			3.4	7.40	4.07
			4	7.55	–
			4.7	7.52	4.08
0	20	350–650	2.8	5.24	
			3.4	5.32	
			4	5.32	
			4.7	5.34	
		250–750	2.8	6.97	
			3.4	7.05	
			4	7.09	
			4.7	7.06	
20	0	350–650	2.8	4.27	
			3.4	4.29	
			4	4.32	
			4.7	4.33	
		250–750	2.8	5.58	
			3.4	5.63	
			4	5.64	
			4.7	5.65	
20	20	350–650	2.8	4.33	
			3.4	4.43	
			4	4.43	

Axial distance (mm)	Radial distance (mm)	Energy window (keV)	Coincidence window (ns)	Absolute sensitivity (^{22}Na source) (%)	System sensitivity (^{18}F source) (%)
			4.7	4.45	
		250–750	2.8	5.78	
			3.4	5.83	
			4	5.90	
			4.7	5.94	

Table 3

Counting rate performance data and scatter fraction.

Phantom	Energy window (keV)	Peak true (kcps at MBq)	Peak NECR (kcps at MBq)	Scatter fraction[a] (%)
Mouse	350–650	2056 at 166.2	1734 at 147.4	7.0 (6.4)
	250–750	2783 at 181.7	2035 at 136.8	10.3 (8.4)
Rat	350–650	910 at 174.7	538 at 131.4	22.9 (21.9)
	250–750	1298 at 177.7	648 at 130.5	33.8 (32.1)

[a]The scatter fraction values indicated in parentheses were computed after the subtraction of intrinsic radiation.

Table 4

Comparison between various Inveon parameters (this study) and those for Focus 120 as reported by two different groups.

Parameter	Inveon	Focus 120[a]	Focus 120[b]
Volumetric resolution (μL)	Center of FOV	Center of FOV	Center of FOV
	2.49[c]	1.94[c]	2.37
	2 cm radial offset	2 cm radial offset	2 cm radial offset
	5.59[c]	7.81[c]	8.08
Absolute sensitivity for a centered point source (%)	350–650 keV, 3.4 ns	350–650 keV, 6 ns	350–650 keV, 6 ns
	6.07	3.8	4.4
	250–750 keV, 3.4 ns	250–750 keV, 6 ns	250–750 keV, 6 ns
	8.12	6.7	6.7
Scatter fraction[d]	Mouse phantom (Φ = 25 mm, *L* = 70 mm)	Mouse phantom (Φ = 30 mm, *L* = 70 mm)	Mouse phantom (Φ = 25 mm, *L* = 70 mm)
	8.4	15.9	12.3
	Rat phantom (Φ = 60 mm, *L* = 150 mm)	Rat phantom (Φ = 60 mm, *L* = 150 mm)	Rat phantom (Φ = 60 mm, *L* = 150 mm)
	32.1	35	26.3
NECR[d] (kcps at MBq)	Mouse phantom 2035 at 136.8	Mouse phantom 869 at 160.58	Mouse phantom 809 at 88.8
	Rat phantom 648 at 130.5	Rat phantom 228 at 122.84	Rat phantom 300 at 149.85

[a]Kim *et al* (2007).

[b]Laforest *et al* (2007).

[c]Listed data were estimated from oversampled axial profiles.

[d]Comparison data are reported at 250–750 keV coincidence window and 3.4 ns coincidence window for Inveon and at 250–750 keV, 6 ns for Focus 120. Data for Focus 120 were taken from table 4 in Kim *et al* (2007).

Φ = cylinder diameter.

L = cylinder length.